

Manufacture of ceramics with high mechanical properties from red mud and granite waste

I. Gonzalez-Triviño✉, J. Pascual-Cosp, B. Moreno, M. Benítez-Guerrero

Departamento de Ingeniería Civil, de Materiales y Fabricación, Universidad de Málaga, (Málaga, Spain)
✉m.isabel_gt@yahoo.com

Received 10 April 2018
Accepted 25 July 2018
Available on line 28 January 2019

ABSTRACT: Red mud (bauxite residue) is an alkaline suspension that is the by-product of alumina production via the Bayer process. Its elevated annual production and the global inventory of red mud determine its valorisation. Granite can be used as a source of fluxing oxides for the ceramic industry, as can the flake-shaped waste generated during the flaming of granite. In this work, a set of ceramic pieces made of red mud and granite waste are prepared and characterised via X-ray diffraction, a hardness test, electron scanning microscopy, a leaching test, and determining open porosity, water absorption, bulk density and flexural strength of the samples. The main crystalline phases in the high-temperature fired products are hematite, pseudobrookite and anorthite; the presence of magnetite reveals their ferrimagnetic character. All samples present high mechanical properties. Leaching results are below critical levels established by regulations.

KEYWORDS: Ceramic; Characterisation; Flexural strength; Mechanical properties; Scanning electron microscopy (SEM).

Citation/Citar como: Gonzalez-Triviño, I.; Pascual-Cosp, J.; Moreno, B.; Benítez-Guerrero, M. (2019) Manufacture of ceramics with high mechanical properties from red mud and granite waste. *Mater. Construcc.* 69 [333], e180 <https://doi.org/10.3989/mc.2019.03818>

RESUMEN: *Fabricación de cerámicas con altas propiedades mecánicas a partir de lodo rojo y residuo de granito.* El residuo de bauxita (lodo rojo) es una suspensión alcalina generada durante el proceso Bayer de producción de alúmina. La elevada producción anual e inventario global determinan su valorización. El granito puede usarse como fuente de óxidos fundentes para la industria cerámica y del mismo modo, el residuo en esquirlas generadas durante el flameado del granito. En este trabajo, se preparan una serie de piezas a partir de lodo rojo y residuo de granito, caracterizadas mediante difracción de rayos X, dureza, microscopía electrónica de barrido y lixiviación, determinando porosidad abierta, absorción de agua, densidad y resistencia a la flexión de las muestras. Las principales fases cristalinas en los productos fabricados a alta temperatura son hematita, pseudobrookita y anortita; la presencia de magnetita revela su carácter ferrimagnético. Todas las muestras presentan elevadas propiedades mecánicas. Los resultados del análisis de lixiviados están por debajo de los niveles críticos establecidos en normativa.

PALABRAS CLAVE: Cerámica; Caracterización; Resistencia a la flexión; Propiedades mecánicas; Microscopía electrónica de barrido (MEB).

ORCID ID: I. González-Triviño (<https://orcid.org/0000-0002-0012-2425>); J. Pascual-Cosp (<https://orcid.org/0000-0001-5082-5957>); B. Moreno (<https://orcid.org/0000-0002-7453-7981>); M. Benítez-Guerrero (<https://orcid.org/0000-0002-0489-5636>)

Copyright: © 2019 CSIC. This is an open-access article distributed under the terms of the Creative Commons Attribution 4.0 International (CC BY 4.0) License.

1. INTRODUCTION

Red mud is the residue generated during the Bayer process, which produces alumina from bauxite. Due to the way the alumina is extracted, the red mud generated constitutes an alkaline solution with a pH between 10 and 13. The annual residue production is estimated to be over 100 million tonnes (Mtpa) and the global inventory reached an estimated 3.5 billion tonnes (Bt) in 2014 (1).

Nowadays, discharging red mud into the sea is avoided (2), as the seabed near the point of discharge can be altered (3-5). Far from solving the problem, however, methods for storing red mud contribute to environmental and safety risks (6,7).

The great amount of mud generated during the process and its accumulated value determine the importance of its valorisation. Different solutions for using red mud have been presented (8-14), but its use in the fabrication of building elements is the most widespread solution, as this industry needs large quantities of raw materials. In this field, red mud is used as a starting material, along with traditional compounds like clay, silica or lime. There are several studies that endorse the use of red mud in concrete or cement (15) and in ceramic manufacture (bricks, tiles) (16,17), all of them meeting the required industrial standards.

The flaming of granite generates a flake-shaped residue which has barely been altered compositionally or morphologically, and thus these flakes could be used as a source of fluxing oxides, like feldspars, for the ceramic industry. The flakes are landfilled in the surroundings of the granite processing plant due to the perception that the risk of contamination is low. The production of granite waste can be estimated to be 22 Mtpa, taking in consideration that the amount of waste generated during industrial cutting and processing is 65% (18) of the total granite production (19).

Choosing this material provides an outlet for a residue that is rarely used. Most research on the utilisation of granite waste is limited to the use of the slurry from the cutting/polishing processes or crushed granite itself as aggregate in the production of concrete and ceramic tiles (20,21).

In this paper, the use of red mud and granite flakes from flaming (a treatment that confers a rustic finish to the granite surface) is presented as an option for changing an unused residue which is usually landfilled around transformation points into a raw material for producing ceramic tiles with high mechanical properties. These properties will provide a high added value to the final products.

2. MATERIALS AND METHODS

A set of samples (10 mm × 80 mm × 10 mm) were prepared using different quantities of the wastes taken as raw materials in this work: red mud from the Alcoa

plant in San Ciprián (Lugo, Spain) and residues from the flaming of granite. The red mud was air dried and ground to obtain a fine dust with homogeneous granulometry. The granite flakes were milled in a Fritsch Pulverisette 7 ball mill with tungsten carbide jars, and later they were sieved in a 75 micron mesh.

For this work, the selected red mud/granite waste proportions (% w/w) were 50/50, 60/40 and 70/30. The green ceramic bodies were formed by uniaxially pressing the dry dust with a hydraulic Perkin-Elmer press of 15 Tn and under a load of 10 tons for 90 seconds.

The calcination treatment consisted of: a heating rate of 10 °C/min, from room temperature to 573 °C; a soaking time of 10 minutes; a heating rate of 10 °C/min to maximum firing temperature; a soaking time of 30 minutes; a cooling rate of 5 °C/min to 573 °C; a soaking time of 5 minutes; free cooling from 573 °C to room temperature. Maximum firing temperatures were: 1100 °C, 1150 °C, 1160 °C and 1170 °C. For the hardness test and scanning electron microscopy (SEM), the ceramic pieces were polished to a specular finish using a Buehler Phoenix Beta automatic polisher at 500 rpm for 5 minutes with each cloth and diamond paste (9 micron to 1 micron).

The specimens were named according to the percentage of red mud in the paste: LG50, LG60 and LG70.

2.1. Mechanical characterisation methods and techniques

A flexural strength test was conducted following the method described by ISO standard 10545-4 (22). The equipment used was an MTS 809 test system with a displacement speed of 0.005 mm/s.

Vickers hardness measurements were obtained in accordance with the UNE-EN 843-4:2005 standard (23), employing a Matsuzawa MXT70 microhardness tester with an incorporated optical microscope. An adequate number of indentations were made under a load of 1 kgf (9.8 MPa) for 40 s.

2.2. Compositional and morphological characterisation techniques

The chemical composition of the raw materials was determined by x-ray fluorescence (XRF), using a 4 kW sequential wavelength-dispersive X-ray spectrometer (Philips Magix PRO PW-2440).

In the case of the red mud and the ceramic products, powder x-ray diffraction (XRD) was performed on a Bruker D8 diffractometer, using MoK α 1 radiation (0.907300 Å) and a LYNXEYE XE detector. The recorded diffraction angle was from 1° to 35° (2 θ). For the granite residue, a PANalytical X'Pert PRO MPD diffractometer was used, with CuK α 1 radiation (1.5406 Å) and an X'Celerator RTMS detector. The recording was done with a diffraction angle of 10° to 80° (2 θ).

Water absorption, open porosity and bulk density were evaluated according to the UNE-EN ISO 10545-3 standard (24). Five samples were used for this determination.

The morphology of the raw materials and the final products was analysed via SEM using a JEOL JSM-6490 LV, with a Si(Li) Oxford Inca X-Sight detector for energy dispersive x-ray spectroscopy (EDX). Prior to analysis, the samples were gold-sputtered in order to avoid surface charging.

The leaching test was performed according to the UNE-EN 12457-4 standard (25). Distilled water was used as the leaching liquid. The conductivity and the pH of the leachate were measured with an Oakton PC 510 tester. The leachate analysis was performed with a Nexion 300D inductively coupled plasma mass spectrometer (ICP-MS) by Perkin Elmer.

3. RESULTS AND DISCUSSION

3.1. Raw materials characterisation

The raw material compositions as determined by XRF were presented in Table 1. While the red mud presented high iron oxide (47.35%) and alumina (19.99%)

content, as well as significant titanium oxide content (9.81%), the granite waste was rich in silica (67.73%) and alumina (14.19%) with a relatively high content of fluxing oxides that promote sintering.

The XRD analysis in Figure 1 shows that red mud mainly consisted of hematite, goethite, boehmite, calcium iron aluminium silicate and rutile. Quartz, calcite, natrodavynite, sodium aluminium silicate and magnetite were present in lesser amounts. In the case of granite, the main components were quartz, albite, anorthoclase, biotite and muscovite; other phases occurring in a lesser amount were orthoclase and sodium aluminium silicate.

3.2. Physical and mechanical properties of the specimens

The generation of open porosity depended on both composition and temperature, as Figure 2 shows. Thus, up to 1150 °C open porosity decreased with temperature via densification due to the higher formation of glassy phase. Above this temperature, open porosity increased with temperature due to the generation of oxygen during the reduction of iron from red mud, confirmed by a density decrease that is more pronounced as the red mud content increased.

TABLE 1. X-ray fluorescence of the starting materials (%)

	Fe ₂ O ₃	Al ₂ O ₃	TiO ₂	Na ₂ O	SiO ₂	CaO	P ₂ O ₅	MgO	K ₂ O	Pb ₂ O ₅	MnO
Red mud	47.35	19.99	9.81	8.31	7.42	6.16	0.45	0.33	0.11	–	0.07
Granite waste	3.69	14.19	0.66	3.16	67.73	4.18	–	0.77	5.32	0.30	–

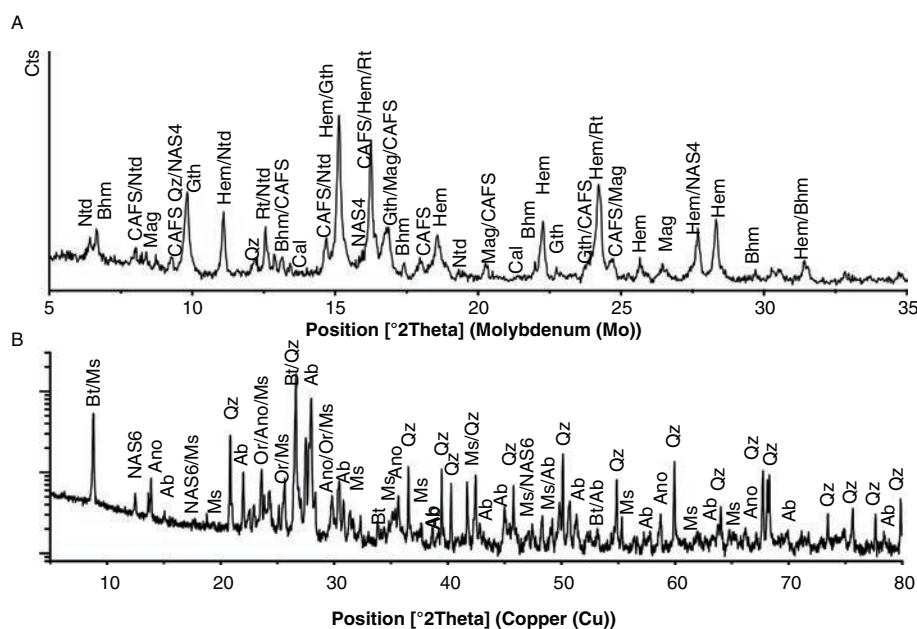


FIGURE 1. Powder X ray diffraction for red mud (A) and granite waste (B). Ab: albite, Ano: anorthoclase, Bt: biotite, Bhm: boehmite, Cal: calcite, CAFS: calcium aluminium iron silicate hydroxide (Ca₃AlFe(SiO₄)(OH)₈), Gth: goethite/aluminous goethite, Hem: hematite, Mag: magnetite, Ms: muscovite, NAS4: sodium aluminium silicate (Na₄Al₂Si₂O₉), NAS6: sodium aluminium silicate (Na₆Al₆Si₁₀O₃₂), Ntd: natrodavynite, Or: orthoclase, Qz: quartz, Rt: rutile.

As this process was happening, some pores were closed by the formation of the glassy phase; however, as the red mud content increased, the glassy phase content was limited (a smaller amount of granite) and could not close all of the pores that the gas opened when being released, so this favoured better pore interconnection. In the LG50 sample, this porosity effect got masked by the densification produced by the formation of larger amounts of glassy phase provided by the granite, closing pores and their interconnections. The increase of glassy phase was favoured by the presence of alkali-feldspars (albite, anorthoclase, orthoclase, sodium aluminium silicate) in the granite.

Figure 2 also shows the vitrification temperatures of the samples, marked as the points where the water absorption and linear shrinkage lines cross. As the figure shows, the temperature at which vitrification began increased with the amount of red mud content in the paste: LG50 begins at 1135°C, LG60 at 1140°C and LG70 at 1150°C.

Water absorption was directly related to the porosity developed during sintering. It can, therefore, be considered a simple way to predict the technological properties of the final products. These results match those for bulk density, except for the case of LG50, as shown in Figure 3. It has been pointed out that the formation of closed pores is responsible for this behaviour (26). Dense phases like hematite, which comes from red mud, were responsible for the higher bulk density in samples

rich in bauxite residue. The bulk density values varied between 2.00 g/cm³ and 2.25 g/cm³.

Soaking times were introduced in the firing process at 573 °C to 1) facilitate the polymorphic transformation of quartz from phase α to the more reactive phase β during the heating process and 2) minimise the stress originating during the cooling process from the reduction of volume due to the transformation of quartz from phase β to phase α . Thus, the presence of a more reactive phase of quartz led to the best densification of the specimens by generating a greater amount of glassy phase, while mechanical behaviour was improved by the reduction of stress during the cooling process.

One of the most representative properties of the mechanical behaviour of a ceramic material is flexural strength. The densification of samples led to better mechanical behaviour, with higher flexural strength (Figure 4); for samples LG60 and LG70, a decrease in density and the formation of iron aluminium silicates (augite, hornblende) led to lower flexural strength (27). Amphiboles (hornblende) and pyroxenes (augite) developed from biotite during the firing process, as described by Bowen's reaction series.

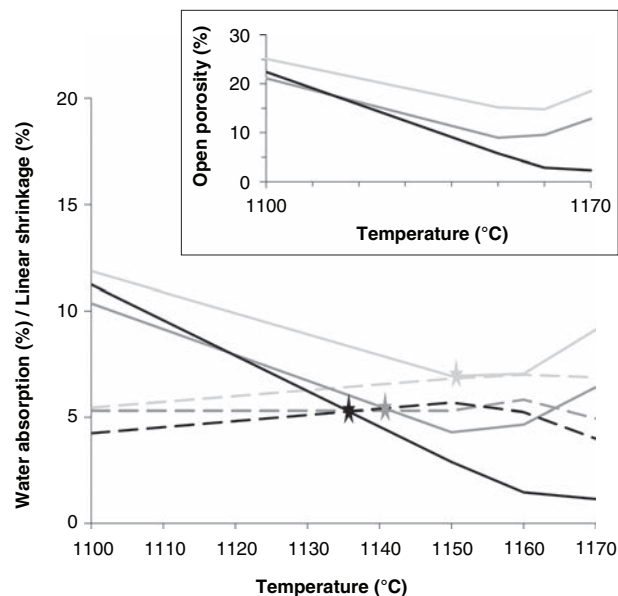


FIGURE 2. Water absorption (solid line) and linear shrinkage (dashed line) according to the final firing temperature. Inset: Open porosity according to the final firing temperature. Black line: LG50; Dark grey line: LG60; Light grey line: LG70.

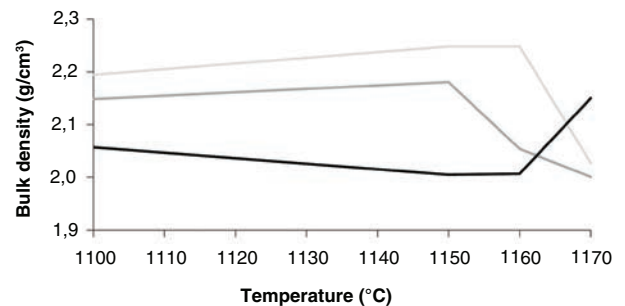


FIGURE 3. Bulk density according to the final firing temperature, g/cm³. Black line: LG50; Dark grey line: LG60; Light grey line: LG70.

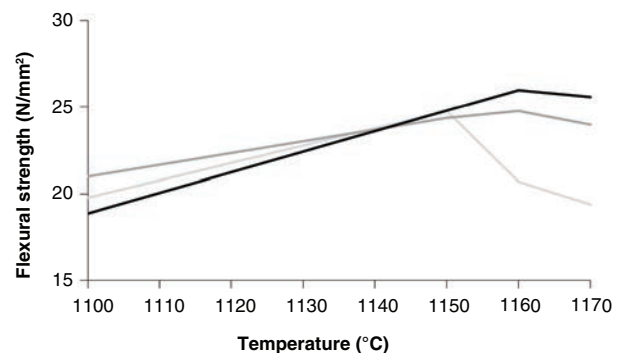


FIGURE 4. Flexural strength according to the final firing temperature, N/mm². Black line: LG50; Dark grey line: LG60; Light grey line: LG70.

3.3. Analysis of selected high-strength specimens

From the results, it can be deduced that the specimens with better mechanical properties (high flexural strength and low water absorption) were those that were sintered at 1150 °C and above. Moreover, Figure 2 shows that vitrification began near this temperature for the three compositions under study. That is why further study was limited to these samples.

Vickers hardness values for all specimens were 440-550 kgf/mm² (4.3-5.4 GPa), as shown in Table 2. These results depended on densification and on crystallography, and as a higher bulk density and some phases like quartz also increased hardness, the granite content in the paste played an important role in the hardness results.

The mineralogical composition was determined by X-ray diffraction. The main phases for the three studied compositions were: hematite, pseudobrookite, magnetite, sodium anorthite, rutile, nepheline and quartz. A semiquantitative analysis of the fired samples is presented in Table 3. Rutile and nepheline XRD signals became more intense with higher red mud content, whereas granite supplied quartz. Quartz intensity decreased with temperature since it transformed into silicates, providing the formation of the glassy phase and thus the densification and strength of the specimens. This explains the increasing strength in sample LG50. The silicates formed were anorthite, nepheline and augite. The formation of these phases could have been as follows:

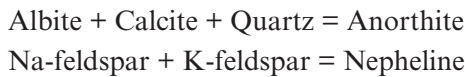
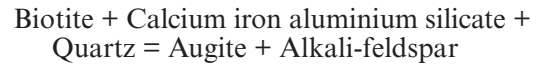
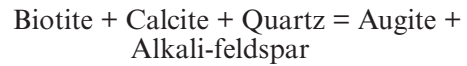


TABLE 2. Vickers micro-hardness values of the specimens at 1150°C, 1160 °C and 1170°C (kgf/mm²)

Temperature	1150 °C	1160 °C	1170 °C
LG50	504.1	513.5	519.0
LG60	545.6	507.5	449.9
LG70	446.9	475.3	354.8



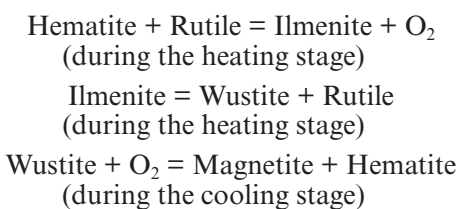
The presence of magnetite in the final products was evidence of their ferrimagnetic character, as magnetite is a ferrimagnetic mineral itself. Even though magnetic properties were not an object of study in this work, the samples were subject to an empirical test, proving that they were attracted by a magnet. The content of magnetite in the fired products varied from 5.1% to 12.3%, as presented in Table 3. Even in the case of the smallest value, the magnetite content was enough to justify the ferrimagnetic character of the ceramics.

Although it could not be identified in the diffractions, ilmenite might have been formed during the firing. The development of ilmenite in the process is essential to explaining the presence of pseudobrookite in the fired samples, as other researchers have found previously (28). The possibility that cations like magnesium entered the crystal lattice of pseudobrookite produced a thermal stabilisation of this phase, since the eutectoid of these solid solutions is located at lower temperatures than the pure aluminium titanate solution (28, 29). Furthermore, the formation of magnetite can be similarly explained through the oxidation of wustite from the decomposition reaction of ilmenite. Wustite in the oxidising furnace atmosphere during the cooling stage leads to the formation of magnetite and hematite (30).

The formation of ilmenite from hematite and rutile happened during the heating stage, where a local reducing environment around the samples was created by the diffusion of air to the upper part of the furnace and helped by the release of CO₂ from the decomposition of carbonated phases (calcite and natrodavynite). When the temperature increased, ilmenite decomposed. During the cooling stage, the environment around the samples became oxidising and magnetite and hematite were generated from wustite.

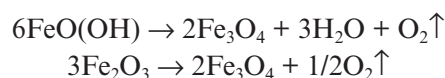
TABLE 3. Semiquantitative analysis of fired samples (%)

Temperature (°C)	LG50				LG60				LG70			
	1100	1150	1160	1170	1100	1150	1160	1170	1100	1150	1160	1170
An	43.3	43.2	42.0	41.5	38.8	39.4	37.1	35.4	28.2	26.9	23.8	23.2
Hem	18.0	20.2	21.0	22.3	20.9	23.6	24.1	26.0	28.0	29.5	29.1	27.7
Mag	6.2	5.1	5.5	5.4	6.7	5.4	6.1	6.2	10.4	10.9	11.1	12.3
Psb	8.2	9.2	9.4	10.5	9.4	10.6	12.2	13.7	9.2	9.2	10.1	12.0
Qz	12	11.3	10.8	10.0	10.8	9.6	8.2	7.3	8.2	6.4	5.9	5.2
Rt	3.3	2.9	2.8	3.1	4.3	2.9	3.1	3.2	4.1	3.3	3.6	3.9
Nph	7.9	8.2	8.5	7.2	9.1	8.6	9.1	8.4	11.9	13.8	16.4	15.6



Scanning electron microscopy shows the morphological and compositional heterogeneity of the samples. Figure 5 shows that all the specimens were highly porous, with a pore size of about 20-200 nm. The number and average size of the pores increased with the granite content in the paste. Although most of porosity was closed porosity, the number of open pores was not negligible, particularly in the LG70 specimens. Open porosity decreased as the temperature rose in the case of the LG50 samples, as the glassy phase was formed. On the contrary, in the specimens with more red mud content the formation of the glassy phase was not enough to offset the effect of the oxygen generated by the reduction of iron. The release of oxygen was produced during the process of reducing Fe^{3+} to Fe^{2+} , and with the increase of temperature the iron-rich phases in red mud reacted and gas was emitted. Dehydration of goethite to hematite presented magnetite as an intermediate compound, so part of the Fe^{3+} reduced to Fe^{2+} (31). Furthermore, hematite transformation

to magnetite contributed to this oxygen release as well (32).



These results can be related to the water absorption and bulk density results. The shape of the pores varied with composition and temperature, and thus the more granite there was in the paste or the higher the firing temperature was, the more rounded the pores were. The presence of different phases was demonstrated by the different tones of the back-scattered electron compositional images (BEC) in Figure 5, and these can be identified by energy-dispersive x-ray spectroscopy (EDX) of the selected points marked in the images (Table 4).

According to the EDX and XRD data, in specimen LG50 fired at 1150 °C, area 1 was compatible with an aluminium-hematite or hematite supported in aluminium silicate matrix. However, area 2 was characterised by a high content of silicon, much higher than aluminium, so it was composed of a vitreous matrix and some quartz. At 1160 °C, areas 1 and 2 corresponded to hematite particles with different structures, area 3 seemed to be an aluminium silicate (anorthite) with the presence of hematite, and area 4 presented a composition similar to that of pseudobrookite. When this composition was fired at 1170 °C, area 1 was rich in iron and the amount of titanium could guide the presence of pseudobrookite and rutile. Area 2 was constituted by silicon and oxygen, which corresponds to quartz. In LG70 at 1150 °C, area 1 was constituted by aluminium silicates (anorthite and nepheline) and was enriched in silicon, which may indicate the presence of quartz. The Ti/Fe relation in area 2 indicated the presence of pseudobrookite in an aluminium silicate matrix. At 1170 °C, area 1 for LG70 showed hematite supported in a nepheline/anorthite matrix; while area 2 corresponded to pseudobrookite with a presence of anorthite.

The leaching test determines material stability under ordinary environmental conditions and the release of hazardous elements. The most restrictive standard applicable for this case, the “Guideline for drinking-water quality” published by WHO (33), was used as a reference, along with other considerations where applicable. The pH and conductivity values were within the range to consider the leachate as drinking-water, except in the case of pieces sintered at 1170 °C, where conductivity was above the standard limit values for specimens LG60 and LG70. This could be due to the higher open porosity that these samples presented, which favoured the dissolution of phases inside the piece. Even so, levels in leachates for all the specimens were far below the established limits, so the leaching of samples does not involve any health risk and the structural stability of the material is guaranteed.

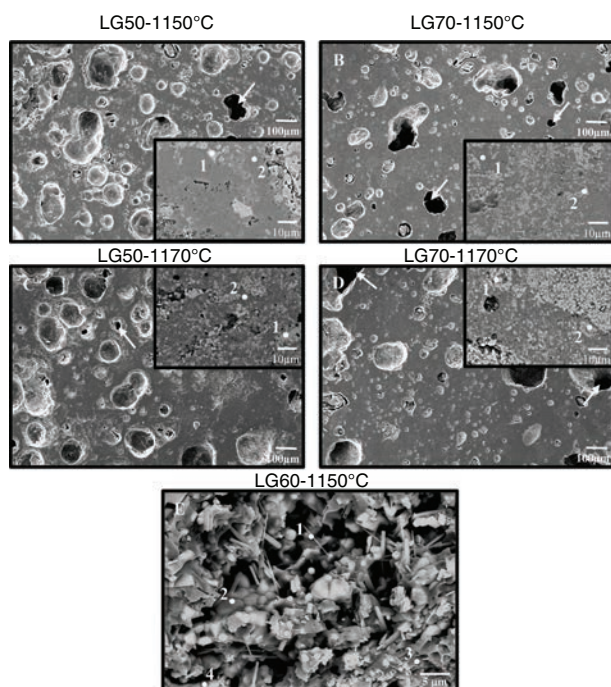


FIGURE 5. A-D: SEM image (SEI) of specimens LG50 and LG70 at 1150 °C and 1170 °C (X100). Scale bar: 100 μm . Inset: BEC image of detail (X2000). Scale bar: 10 μm . Open pores marked by arrows. E: BEC image of fracture view (X3000) of specimen LG60-1150°C. Points show where the EDX analysis were performed.

TABLE 4. Point EDX analysis of selected specimens at 1150 °C and 1170 °C (Atomic%). ND: not detected

			O	Na	Mg	Al	Si	K	Ca	Ti	Fe
1150 °C	LG50	Area 1	48.74	2.32	ND	10.88	3.32	0.40	0.35	1.11	32.87
		Area 2	57.01	4.54	0.02	10.27	21.14	0.59	3.50	0.43	2.50
		Area 1	45.58	2.26	ND	14.08	3.76	0.57	3.77	4.47	25.51
	LG60	Area 2	65.61	2.14	0.37	4.98	1.59	ND	0.44	1.70	23.18
		Area 3	44.92	2.94	0.58	11.23	8.80	0.34	6.86	3.15	21.17
		Area 4	34.52	1.38	0.33	3.15	2.09	ND	0.87	19.62	38.05
1170 °C	LG70	Area 1	60.03	1.16	0.10	7.44	4.72	0.07	1.56	9.10	15.84
		Area 2	58.33	ND	ND	0.06	41.25	0.01	0.04	ND	0.30
	LG50	Area 1	53.45	7.32	0.43	10.36	24.25	1.35	2.49	ND	0.35
		Area 2	45.54	3.17	0.19	4.43	15.03	0.77	11.41	7.17	12.27
	LG70	Area 1	53.37	3.36	0.79	4.39	6.54	0.38	0.45	1.72	29.00
		Area 2	53.61	0.40	3.07	4.54	7.27	0.40	1.47	11.01	18.23

4. CONCLUSIONS

This work has demonstrated that the valorisation of red mud is possible through ceramisation to obtain pieces with high physical and mechanical properties. Specimens with more granite content that have been fired at high temperature (>1150 °C) show the best behaviour due to greater densification, since these are above their vitrification temperature. The main crystalline phases in the fired products are hematite, pseudobrookite, anorthite, rutile, nepheline and quartz; magnetite has been found in all cases, revealing their ferrimagnetic character. SEM-EDX analyses reveal that the specimens present a high degree of sintering and that they are composed of an aluminium silicate matrix that contains small particles and some aggregates of iron and titanium rich phases. ICP-MS of the leachates generated by the materials shows that their release does not involve health or environmental risk, and the stability of the products working under ordinary environmental conditions is guaranteed.

REFERENCES

- Xue, S.; Zhu, F.; Kong, X.; Wu, C.; Huang, L.; Huang, N.; Hartley, W. (2016) A review of the characterization and revegetation of bauxite residues (Red mud). *Environ. Sci. Pollut. Res. Int.* 23 [2], 1120–1132. <https://doi.org/10.1007/s11356-015-4558-8>
- Report of the 28th meeting of the scientific group, International Maritime Organization Publishing, London (UK), (2005).
- Dauvin, J.C. (2010) Towards an impact assessment of bauxite red mud waste on the knowledge of the structure and functions of bathyal ecosystems: The example of the Cassidaigne canyon (North-Western Mediterranean Sea). *Mar. Pollut. Bull.* 60 [2], 197–206. <https://doi.org/10.1016/j.marpolbul.2009.09.026>
- Fabri, M.C.; Pedel, L.; Beuck, L.; Galgani, F.; Hebbeln, D.; Freiwald, A. (2014) Megafauna of vulnerable marine ecosystems in French mediterranean submarine canyons: Spatial distribution and anthropogenic impacts. *Deep Sea Res. II* 104, 184–207. <https://doi.org/10.1016/j.dsr2.2013.06.016>
- Fontanier, C.; Fabri, M.C.; Buscail, R.; Biscara, L.; Koho, K.; Reichart, G.J.; Cossa, D.; Galaup, S.; Chabaud, G.; Pigot, L. (2012) Deep-sea foraminifera from the Cassidaigne Canyon (NW Mediterranean): Assessing the environmental impact of bauxite red mud disposal. *Mar. Pollut. Bull.* 64 [9], 1895–1910. <https://doi.org/10.1016/j.marpolbul.2012.06.016>
- Czövek, D.; Novák, Z.; Somlai, C.; Asztalos, T.; Tiszlavicz, L.; Bozóki, Z.; Ajtai, T.; Utry, N.; Filep, A.; Bari, F.; Peták, F. (2012) Respiratory consequences of red sludge dust inhalation in rats. *Toxicol. Lett.* 209 [2], 113–120. <https://doi.org/10.1016/j.toxlet.2011.12.006>
- Mišík, M.; Burke, I.T.; Reismüller, M.; Pichler, C.; Rainer, B.; Mišíková, K.; Mayes, W.M.; Knasmüller, S. (2014) Red mud a byproduct of aluminum production contains soluble vanadium that causes genotoxic and cytotoxic effects in higher plants. *Sci. Total Environ.* 493, 883–890. <https://doi.org/10.1016/j.scitotenv.2014.06.052>
- Li, G.; Liu, M.; Rao, M.; Jiang, T.; Zhuang, J.; Zhang, Y. (2014) Stepwise extraction of valuable components from red mud based on reductive roasting with sodium salts. *J. Hazard. Mater.* 280, 774–780. <https://doi.org/10.1016/j.jhazmat.2014.09.005>
- Liu, Y.; Zhao, B.; Tang, Y.; Wan, P.; Chen, Y.; Lv, Z. (2014) Recycling of iron from red mud by magnetic separation after co-roasting with pyrite. *Thermochim. Acta* 588, 11–15. <https://doi.org/10.1016/j.tca.2014.04.027>
- Zhang, R.; Zheng, S.; Ma, S.; Zhang, Y. (2011) Recovery of alumina and alkali in Bayer red mud by the formation of andradite-grossular hydrogarnet in hydrothermal process. *J. Hazard. Mater.* 189 [3], 827–835. <https://doi.org/10.1016/j.jhazmat.2011.03.004>
- González-Triviño, I.; Benítez-Guerrero, M.; Carda Castelló, J.B.; Moreno, B.; Pascual-Cosp, J. (2018) Synthesis and characterization of ferrimagnetic glass-ceramic frit from waste. *Int. J. Appl. Ceram. Technol.* 15 [3], 775–782. <https://doi.org/10.1111/ijac.12850>
- Kehagia, F. (2010) A successful pilot project demonstrating the re-use potential of bauxite residue in embankment construction. *Resour. Conserv. Recycl.* 54 [7], 417–421. <https://doi.org/10.1016/j.resconrec.2009.10.001>
- Gray, C.W.; Dunham, S.J.; Dennis, P.G.; Zhao, F.J.; McGrath, S.P. (2006) Field evaluation of in situ remediation of a heavy metal contaminated soil using lime and red-mud. *Environ. Pollut.* 142 [3], 530–539. <https://doi.org/10.1016/j.envpol.2005.10.017>
- Huang, W.; Wang, S.; Zhu, Z.; Li, L.; Yao, X.; Rudolph, V.; Haghseresht, F. (2008) Phosphate removal from wastewater

- using red mud. *J. Hazard. Mater.* 158 [1], 35–42. <https://doi.org/10.1016/j.jhazmat.2008.01.061>
15. Pontikes, Y.; Angelopoulos, G.N. (2013) Bauxite residue in cement and cementitious applications: Current status and a possible way forward. *Resour. Conserv. Recycl.* 73, 53–63. <https://doi.org/10.1016/j.resconrec.2013.01.005>
 16. Rai, S.; Lataye, D.H.; Chaddha, M.J.; Mishra, R.S.; Mahendiran, P.; Mukhopadhyay, J.; Yoo, C.K.; Wasewar, K.L. (2013) An Alternative to Clay in Building Materials: Red Mud Sintering Using Fly Ash via Taguchi's Methodology. *Adv. Mater. Sci. Eng.* 2013, Article ID 757923. <https://doi.org/10.1155/2013/757923>
 17. Pérez-Villarejo, L.; Corpas-Iglesias, F.A.; Martínez-Martínez, S.; Artiaga, R.; Pascual-Cosp, J. (2012) Manufacturing new ceramic materials from clay and red mud derived from the aluminium industry. *Constr. Build. Mater.* 35, 656–665. <https://doi.org/10.1016/j.conbuildmat.2012.04.133>
 18. Singh, S.; Nagar, R.; Agrawal, V.; Rana, A. (2015) Utilization of granite cutting waste in concrete as partial replacement of sand. Conference paper: UKIERI Concrete Congress – Concrete Research Driving Profit and Sustainability, Jalandhar, India.
 19. Ashmole, I.; Motloun, M. (2008) Dimension stone: the latest trends in exploration and production technology. Conference paper: The international conference in surface mining, Johannesburg, South Africa.
 20. Hamza, R.A.; El-Haggar, S.; Khedr, S. (2011) Marble and granite waste: characterization and utilization in concrete bricks. *Int. J. Biosci. Biochem. Bioinforma.* 1 [4], 286–291.
 21. González-Triviño, I.; Benítez-Guerrero, M.; Moreno, B.; Pascual-Cosp, J. (2018) Ferrimagnetic wollastonite ceramics based on waste valorization. *Int. J. Appl. Ceram. Technol.* 00, 1–6. <https://doi.org/10.1111/ijac.13014>
 22. Committee AEN/CTN 138. (2014). UNE-EN ISO 10545-4:2014. Ceramic tiles. Part 4: Determination of modulus of rupture and breaking strength. Madrid: AENOR.
 23. Committee AEN/CTN 264. (2015). UNE-EN 843-4:2005. Advanced technical ceramics. Mechanical properties of monolithic ceramics at room temperature. Part 4: Vickers, Knoop and Rockwell superficial hardness tests. Madrid: AENOR.
 24. Committee ISO/TC 189. (2018). ISO 10545-3:2018. Ceramic tiles. Part 3: Determination of water absorption, apparent porosity, apparent relative density and bulk density. Switzerland: International Organization for Standardization.
 25. Committee AEN/CTN 77. (2002). UNE-EN 12457-4:2002. Characterization of waste. Leaching. Compliance for leaching of granular waste materials and sludges. Part 4: One stage batch test at a liquid to solid ratio of 10 L/kg for materials with particle size below 10 mm (without or with size reduction). Madrid: AENOR.
 26. Torres, P.; Manjate, R.S.; Quaresma, S.; Fernandes, H.R.; Ferreira, J.M.F. (2007) Development of ceramic floor tile compositions based on quartzite and granite sludges. *J. Eur. Ceram. Soc.* 27 [16], 4649–4655. <https://doi.org/10.1016/j.jeurceramsoc.2007.02.217>
 27. Zhao, L.; Li, Y.; Jiang, F.; Cang, D. (2016) Effects of composition changes on the sintering properties of novel steel slag ceramics. In: *Advances in materials science for environmental and energy technologies V*, John Wiley & Sons, Inc., Hoboken, New Jersey (USA), (2016). <https://doi.org/10.1002/9781119323624>
 28. Barrios de Arenas, I.; Arenas, F.; Cho, S.A.; Martínez, S.; Sicardi, R. (2000) Efecto de los aditivos en la formación y estabilidad térmica a baja temperatura del titanato de aluminio. *Bol. Soc. Esp. Ceram. V.* 39 [6], 699–703 (In Spanish). <https://doi.org/10.3989/cyv.2000.v39.i6.768>
 29. Kato, E.; Daimon, K.; Takahashi, J. (1980) Decomposition Temperature of b-Al₂TiO₅. *J. Am. Ceram. Soc.* 63 [5-6], 355–356. <https://doi.org/10.1111/j.1151-2916.1980.tb10745.x>
 30. Zhang, D. (2013) Ultra-supercritical coal power plants. Materials, technologies and optimisation, Woodhead publishing limited, Cambridge (UK), (2013).
 31. Özdemir, Ö., Dunlop, D.J. (2000) Intermediate magnetite formation during dehydration of goethite. *Earth Planet Sci. Lett.* 177 [1–2], 59–67. [https://doi.org/10.1016/S0012-821X\(00\)00032-7](https://doi.org/10.1016/S0012-821X(00)00032-7)
 32. Watanabe, Y., Ishii, K. (1995) Geometrical consideration of the crystallography of the transformation from α-Fe₂O₃ to Fe₃O₄. *Phys. Stat. Solids* 150 [2], 673–686. <https://doi.org/10.1002/pssa.2211500210>
 33. Guidelines for drinking-water quality, World Health Organization, Geneva (CH), (2011).